International Journal of Nanomedicine

Dovepress

open access to scientific and medical research

Open Access Full Text Article

ORIGINAL RESEARCH

Synergistic Therapy Using Doxorubicin-Loading and Nitric Oxide-Generating Hollow Prussian Blue Nanoparticles with Photoacoustic Imaging Potential Against Breast Cancer

Jijun Fu[1,*]
Qianni Wu[1,*]
Yuanye Dang[1,*]
Xueping Lei[1]
Guining Feng[1]
Mingyue Chen[2]
Xi-Yong Yu[1]

[1]The Key Laboratory of Molecular Target & Clinical Pharmacology, School of Pharmaceutical Sciences, The First Affiliated Hospital of Guangzhou Medical University, The Fifth Affiliated Hospital of Guangzhou Medical University, Guangzhou Medical University, Guangzhou, 511436, People's Republic of China; [2]Foshan Nanhai Vocational School of Health, Foshan, 528211, People's Republic of China

*These authors contributed equally to this work

Introduction: Traditional antitumor chemotherapy faces great challenges, such as multi-drug resistance (MDR) and poor penetration into tumor tissues. The newly emerging nitric oxide (NO)-based gas therapy has been recognized to reduce MDR and has improved permeation into tumor tissue.

Methods: In this study, NO-generating prodrug sodium nitroprusside (SNP) was doped to hollow mesoporous Prussian blue (PB) nanoparticles to fabricate NO-generating nanoparticles (NO-PB), which was further loaded with doxorubicin (DOX).

Results: DOX loaded NO-PB (DOX-NO-PB) was released quicker at pH 6 compared with neutral pH, suggesting NO-PB may facilitate the release of loaded drug in acidic tumor tissue. The capacity of NO production by NO-PB was measured, and the results showed the presence of NO in the culture medium from 4T1 cells incubated with NO-PB and inside the cells. NP-PB could be detected by photoacoustic imaging (PAI) in tumor tissue in 4T1 tumor bearing mice, suggesting this nanoparticle may serve as contrast agent for the noninvasive diagnosis of tumor tissues. NO-PB suppressed the growth of tissues in 4T1 tumor bearing mice. DOX-NO-PB showed more potent anti-tumor effects in 4T1 cells and tumor bearing mice compared with free DOX and NO-PB alone, indicating that the combination of DOX and NO-PB exhibited synergistic effects on tumor suppression.

Conclusion: This study provides a novel nanocarrier for gas therapy with additional PAI imaging capacity. This nanocarrier can be utilized for combination therapy of NO and chemotherapeutics which may serve as theranostic agents.

Keywords: gas therapy, nitric oxide, NO, photoacoustic imaging, PAI, sodium nitroprusside, SNP, hollow mesoporous Prussian blue (PB) nanoparticles

Introduction

Gas therapy against cancer is one of the most quickly developing research field. The principle of this therapeutic strategy is the production of gas molecules within the tumor tissues, which led to the suppression tumor growth. These therapeutic gas molecules include carbon monoxide (CO),[1–4] hydrogen sulfide (H_2S)[5–9] and nitric oxide (NO).

NO is a double-edged sword that functions as a signaling molecule regulating neurotransmission and smooth muscle relaxation under physiological conditions, and may lead to apoptosis of cell as a free radical. Increased NO has been

Correspondence: Jijun Fu
Email fujj@gzhmu.edu.cn

Received: 8 July 2021
Accepted: 16 August 2021
Published: 31 August 2021

recognized to damage DNA and mitochondrial. As a result, gas therapy based on NO has been employed to treat cancers.[10–36] In addition, the vasodilation effect of NO was believed to increase the blood flow in malignant tissues and facilitate drug accumulation in tumors, eventually improving the chemotherapy effects.[10] Furthermore, NO therapy has been reported to inhibit the production of dense stroma in pancreatic ductal adenocarcinoma and breast cancer[11,12] and promote tumor collagen depletion by activating endogenous matrix metalloproteinase.[13] This reduced the compactness of tumor tissue and facilitated the intratumoral penetration of the drug-loading nanocarrier. NO has been also recognized as a potent P-glycoprotein modulator which may help reduce multi-drug resistance (MDR) of chemotherapy.[14,15,33] Furthermore, NO is supposed to inhibit metastasis through blocking the epithelial to mesenchymal transition (EMT).[16–18] Taking all the above mechanisms into account, it is believed that NO possesses antitumor effects by its toxicity and improves the effects of chemotherapy by the MDR reversal, the metastasis inhibition as well as enhancing the accumulation and penetration of pharmaceuticals in the malignant tissues due to the tumor microenvironment modification.

Considering the above advantages of NO, this work aims to combine chemotherapy with gas therapy based on NO. However, since NO has a short half-life in solution or plasma (1.5–6 min), it remains a great challenge to deliver NO into the biological systems. To solve this problem, numerous NO-donors defined as NO-releasing small molecules or functional moieties have been developed and applied for continuous NO release in the target site. The pro-drug nitroglycerin and sodium nitroprusside (SNP) are the most widely used NO-releasing small molecules. Several NO-releasing moieties have been proposed, such as organic nitrates/nitrites,[10,12] S-nitroglutathione (GSNO),[19,29,31] S-nitrosothiols (SNO),[14,32,35] Roussin's black salt,[25,28,33] N-diazeniumdiolate (NONOate),[20] L-arginine (L-Arg)[26,34] and S-nitroso-N-acetylpenicillamine (SNAP).[11] However, the short half-life in blood and poor enrichment in tumors restrict their potential use in vivo. Accordingly, suitable delivery systems that can carry NO-donors to the target sites are urgently needed.

Prussian blue (PB), with the general formula of $Fe_4[Fe(CN)_6]_3$, has been approved by US Food and Drug Administration for treating radioactive exposure and scavenging the harmful metal ions from body. Its good biosafety has been demonstrated in clinical practice. The hollow mesoporous PB nanoparticles have attracted increasing attention due to the good physiological stability, the excellent drug-loading capacity and the satisfying photoacoustic imaging (PAI) feature.[37–39] The mesoporous PB shows superior physiological stability in the blood to the raw PB.[40] In addition, the mesoporous PB displays good drug-loading capacity due to its hollow structure. Moreover, comparable to the raw PB, the mesoporous PB exhibits appealing PAI feature attributing to the strong absorbance in the near-infrared (NIR) region.[40–43] PAI is a newly developed diagnostic technology, it has the advantages of both ultrasound imaging and optical imaging with high resolution, excellent sensitivity and the ability of real-time imaging. PAI has been used to monitor both the tumor progression and the therapy response in a non-invasive fashion. The mesoporous PB carrying anticancer drug could be used for cancer theranostics. The accurate identification of tumor size and location confers a real-time monitor of the therapeutic effect.

Sodium nitroprusside (SNP) can be metabolized in the body to release NO. It is widely used to treat acute heart failure and hypertensive emergency. SNP, with the general formula of $Na_2Fe(CN)_5NO$, has similar structure to potassium ferricyanide ($K_3Fe(CN)_6$), which is used to prepare the mesoporous PB. Inspired by this, in this work, the authors embedded SNP in the crystal structure of mesoporous PB to prepare SNP-doped mesoporous PB (NO-PB). And, the anticancer doxorubicin (DOX) is encapsulated in the hollow structure of NO-PB. It is hypothesized that the use of NO-PB will overcome the short half-life limitation of the NO-donors and successfully deliver NO to tumor tissues. After metabolism, the produced NO and the released DOX will play synergistic anticancer effects. And, the NO-PB will confer the PAI imaging capacity to this nanoparticle system. In a word, the aim of this work is to design a SNP-doped mesoporous PB nanoparticles that integrate PAI diagnosis and combination therapy including chemotherapeutic and NO-based gas therapy (Figure 1).

Experimental Section

Materials

The polyvinylpyrrolidone (PVP, M. W. 18,000), potassium ferricyanide ($K_3Fe(CN)_6$), sodium nitroprusside (SNP), concentrated hydrochloric acid (HCl), doxorubicin (DOX), sodium dodecyl sulfate (SDS) and 3-(4,5-dimethylthiazol-2-yl)-2,5-diphenyltetrazolium bromide (MTT) were purchased from Aladdin Company (Shanghai, China). The

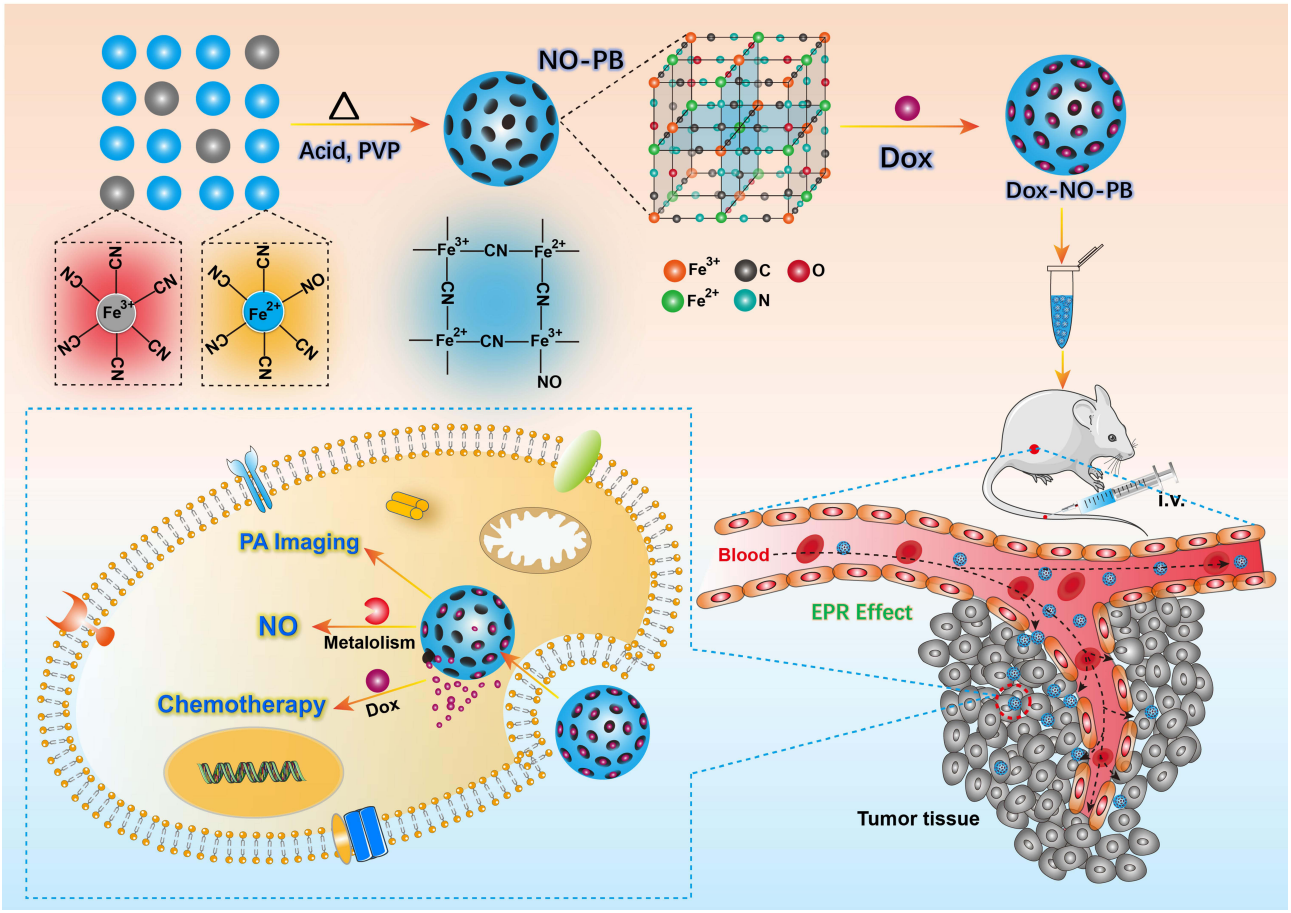

Figure 1 The schematic illustration of this work.

fluorescence probe DAF-FM DA, GreenNuc, the Annexin V-FITC/PI kit, the Calcein/PI kit, the Griess kit and Hoechst 33,342 were purchased from Beyotime Corporation (Shanghai, China). The rabbit anti-Ki67 and anti-cleaved caspase 3 primary antibodies and the anti-rabbit secondary antibody were bought from Servicebio Company (Wuhan, China).

Synthesis of PB and NO-PB

To prepare the hollow PB, 200 mg of PVP and 100 mg of $K_3Fe(CN)_6$ were dissolved in 10 mL of deionized water. Then, 100 μL of concentrated hydrochloric acid was added while stirring. The solution was stirred in water bath at 85°C for one hour. After the clear solution changed to blue nano-dispersion, it was cooled to room temperature, and then, sent to dialysis in deionized water or saline for 48 h (cutting molecular weight: 30,000). To prepare the hollow NO-PB, 200 mg of PVP, 15 mg of $K_3Fe(CN)_6$ and 120 mg of SNP were dissolved in 10 mL of deionized water. Then, 100 μL of concentrated hydrochloric acid was added while stirring. The solution was stirred in water bath at 85°C for one hour. After the clear solution changed to blue nano-dispersion, it was cooled to room temperature, and then, sent to dialysis in deionized water or saline for 48 h (cutting molecular weight: 30,000).

Drug Loading

To prepare DOX-NO-PB, 2 mL of DOX water solution (10 mg/mL) was added dropwise to 5 mL of the above NO-PB while stirring, and, the mixture was further stirred for 48 h. Then, the mixture was sent to dialysis in deionized water or saline for 12 h to remove free DOX (cutting molecular weight: 30,000). The drug concentration in DOX-NO-PB was measured by high performance liquid chromatography (HPLC) method. C18 column (5 μm, 20 cm, Xbridge, Waters, U. S. A.) was used, the mobile phase was SDS solution (dissolving 1.44 g of SDS and 0.68 mL of phosphoric acid in 500 mL deionized water) – acetonitrile – methanol (500:500:60). The detection wavelength was 254 nm (SPD-10A, Shimadzu, Japan) and the

flow rate was 1 mL/min (LC-10AT, Shimadzu, Japan). The sample was prepared as follows: 20 μL of the above DOX-NO-PB was added into 180 μL of Na_2CO_3 solution (5 mg/mL) to completely hydrolyze NO-PB; then, 1.8 mL of methanol was added and the clear solution was passed through 0.22 μm filter to get the sample solution. The injection volume was 20 μL. The drug concentration in DOX-NO-PB was calculated according to Equation 1:

$$\text{DOX concentration (mg/mL)} = \text{DOX concentration in sample solution}(\mu g/mL) \times 100/1000 \quad (1)$$

The encapsulation efficiency was calculated according to Equation 2:

$$\text{Encapsulation efficiency}(\%) = \frac{\text{DOX concentration}(mg/mL) \times \text{DOX-NO-PB volume}(mL)/20(mg)}{\times 100} \quad (2)$$

Characterization of the Nanoparticles

Transmission electron microscope (TEM) was used to scan the morphology of the hollow PB, NO-PB and DOX-NO-PB (JEM 2100F, JEOL, Japan), the voltage was 200 kV. Selected area electron diffraction (SAED) was used to characterize the crystals of the nanoparticles. The size and charge of PB, NO-PB and DOX-NO-PB were further featured by ZetaSizer (Malvern, U. K.). The successful formation of NO-PB was validated by X-ray diffraction (XRD) and infrared (IR) spectrum (Tensor II, Bruker, Germany). The voltage in XRD was 40 kV and the current was 40 mA (D8 advanced, Bruker, Germany). The BET test was used to measure the pore distribution in the NO-PB (TriStar 3020, Micromeritics, U. S. A.). Before the test, 128.7 mg of the sample was degassed at 100°C for 5 h. The encapsulation of DOX in DOX-NO-PB was demonstrated by the ultraviolet-visible (UV) spectrum (UV-2600, Shimadzu, Japan).

DOX Release Test

The release of DOX from DOX-NO-PB was measured by dialysis method. In detail, 1 mL of DOX-NO-PB (DOX concentration: 1 mg/mL) was placed in the dialysis bag (cutting molecular weight: 30,000), the dialysis bag was immersed into 19 mL of the release media (tris buffer with pH value of 7.4 or 6.0). Then, the device was placed in a shaker at the temperature of 37°C and the shaking speed was 100 rpm. There were four samples in each group (n = 4). At the time points of 0.25, 0.5, 1, 1.5 and 2 h, 0.5 mL of the release media was withdrawn and the drug concentration was analyzed by HPLC method as described in the "Drug loading" section.

NO Generation in the Cells

4T1 mouse breast cancer cells purchased from the National Infrastructure of Cell Line Resource (Beijing, China) were used in the experiments. The cells were cultured in Dulbecco's modified Eagle media (DMEM) at 37°C, with CO_2 content of 5%. The NO generation in the cells was investigated by two methods, using the Griess reagent and the fluorescence probe DAF-FM DA.

10 x 10^4 of 4T1 cells were seeded in 24-well plate and were cultured overnight for cell attachment. Then, NO-PB was added to the cells to make a final concentration of 25 μg/mL, and NO-PB was also added to fresh media without cells as a control. The conditioned media of 4T1 cells without NO-PB was used as another control. After incubation for 24 h, 100 μL of the media was collected and the Griess reagent was added according to the kit protocol. After reaction for 30 min, the samples were pictured and analyzed by UV spectrum (UV-2600, Shimadzu, Japan).

10 x 10^4 of 4T1 cells were seeded in 24-well plate and were cultured overnight for cell attachment. Then, PB or NO-PB was added to the cells to make a final concentration of 25 μg/mL, the cells without any treatment were used as control. 12 hours later, the culture media was discarded, the cells were washed by PBS for three times and the fresh media was added. Then, the commercial reagent DAF-FM DA (Beyotime biotechnology, China) as cellular NO probe was added in the media for 0.5 h according to the protocol. At last, the NO generation in the cells was imaged by the inverted fluorescence microscope (DMi8, Leica, Germany). The excitation and emission wavelength was 450–490/515 nm. The NO generation in the cells was also measured by the flow cytometer (Cytoflex, Beckman, USA). The process was similar: the cells were collected by trypsinization after incubation with DAF-FM DA, and then, washed by PBS twice. At last, the cells were analyzed using the 488-nm laser.

The Therapeutic Effects Against the 4T1 Cells

10 x 10^4 of 4T1 cells were seeded in 24-well plate and were cultured overnight for cell attachment. Then, PB or NO-PB was added to the cells to make a final

concentration of 50 μg/mL, the cells without any treatment were used as control. 24 hours later, the culture media was discarded, the cells were washed by PBS for three times and the fresh media was added. Then, the commercial reagent GreenNuc (Beyotime biotechnology, China) as caspase 3 activation indicator was added in the media for 0.5 h according to the protocol. At last, the cells were washed by PBS for three times and the caspase 3 activation in the cells was imaged by the inverted fluorescence microscope (DMi8, Leica, Germany). The excitation and emission wavelength was 450–490/515 nm. As the auto-fluorescence of DOX strongly influenced the results' observation, DOX and DOX-NO-PB were not tested.

10 x 10^4 of 4T1 cells were seeded in 24-well plate and were cultured overnight for cell attachment. Then, PB or NO-PB was added to the cells to make a final concentration of 50 μg/mL, the cells without any treatment were used as control. 24 hours later, the culture media was discarded, the cells were washed by PBS for three times and the fresh media was added. Then, the commercial reagent Calcein/PI (Beyotime biotechnology, China) was added in the media for 0.5 h according to the kit protocol. At last, the live and dead cells were imaged by the inverted fluorescence microscope (DMi8, Leica, Germany). The excitation and emission wavelength was 450–490/515 nm for Calcein and 510–550/575 nm for PI. The cell death was also analyzed by the flow cytometer (Cytoflex, Beckman, USA). The PB and NO-PB were added to the cells to get a final concentration of 100 μg/mL. The cells without treatment were used as control. After further incubation for 24 h, the cells were collected by trypsinization and washed by PBS once. Then, the Annexin V-FITC/PI reagents were added according to the kit protocol before analysis. The 488-nm laser was used for Annexin V-FITC and the 561-nm laser for PI. As the auto-fluorescence of DOX strongly influenced the results' observation, DOX and DOX-NO-PB were not tested.

3 x 10^4 of 4T1 cells were seeded in 96-well plate and were cultured overnight for cell attachment. Then, DOX, PB, NO-PB, DOX-NO-PB were added to the cells to get a serial DOX concentrations of 1, 2, 5, 10, 20 μg/mL, and/or NO-PB concentrations of 5, 10, 25, 50, 100 μg/mL. The cells without any treatment were used as controls (n=6). After 24 hours, the cells were washed by PBS twice and cultured in fresh media. The cell viability was measured by MTT method, and the detection wavelength was 490 nm (Epoch, Biotek, USA).

Photoacoustic Imaging (PAI)

Balb/c mice were used in this experiment. The mice were fed in SPF environment and given free access to food and drinking water. All the animal experiments were approved by the Ethic Committee of Guangzhou Medical University (S2020-084) and was performed in accordance with Institutional Guidelines and the Guide for the Care and Use of Laboratory Animals (NIH publication No. 85-23, revised 1996).

The NO-PB with a concentration of 0.6 mM was used as the in-vitro PAI sample, and deionized water was used as a control. The Vevo LAZR-X system (VisualSonics, Canada) was employed, the frequency was 30 MHz and the laser wavelength was 700 nm.

For the in-vivo PAI, to establish tumor bearing mouse model, one million of 4T1 cells in 200 μL of PBS was subcutaneously (s. c.) injected into the 6–8 weeks old female mice armpit. When the tumor grew to about 200 mm^3 according to the equation: volume = length x $width^2/2$, the PAI images of the tumor site were captured. The Vevo LAZR-X system was employed, the frequency was 30 MHz and the laser wavelength was 700 nm. Then, 100 μL of NO-PB (2.5 mg/mL) in saline was intravenously (i. v.) administered to the mice through tail vein. After four hours, the PAI images of the tumor site were captured again to see if signal enhancement happened.

The Antitumor Experiments in Animals

Balb/c mice were used in this experiment. The mice were fed in SPF environment and given free access to food and drinking water. All the animal experiments were approved by the Ethic Committee of Guangzhou Medical University (S2020-084) and was performed in accordance with Institutional Guidelines and the Guide for the Care and Use of Laboratory Animals (NIH publication No. 85–23, revised 1996).

One million of 4T1 cells in 200 μL of PBS was subcutaneously (s. c.) injected into the 6–8 weeks old female mice armpit to establish tumor-bearing mouse model. When the tumor grew to about 100 mm^3 according to the equation: volume = length x $width^2/2$, the mice were divided into four groups: PBS group, DOX solution group, NO-PB group and DOX-NO-PB group. There were five mice in each group (n = 5). 100 μL of PBS, DOX solution, NO-PB or DOX-NO-PB was i. v. given to the mice, the corresponding dose of DOX and/or NO-PB was 50 μg and 250 μg for each mouse. The mice were

treated every other day and four times in total. The tumor volume and body weight of the mice were measured throughout the experiment to reflect antitumor effects and systemic toxicity of the treatments. At the end of the experiment, the mice were sacrificed and the tumor tissues were pictured and weighed. Furthermore, the tumor samples were frozen sectioned and immunohistochemical (IHC) tests of the Ki67 cell proliferation marker and the cleaved caspase 3 cell apoptosis marker were carried out. Moreover, to further assess the systemic toxicity of the treatments, the main organs of heart, liver, spleen, lung and kidney were paraffin sectioned and H

& E staining were performed.

Statistic Analysis

All values were expressed as mean ± standard deviation (SD). All comparisons were performed by the one – way ANOVA *t*-test. A p-value less than 0.05 was taken as statistically significant.

Results and Discussions

Characterization of PB, NO-PB and DOX-NO-PB

PB and NO-PB were simply prepared by one-pot synthesis. Both nanoparticles in saline solution are blue. The morphology of the nanoparticles was characterized by the TEM, and the size and surface zeta potential were further analyzed by dynamic light scattering (DLS) method. As shown in the TEM images (Figure 2A), both PB (right) and NO-PB (left) had porous spherical structure. The hollow structure is an important prerequisite of the excellent drug-loading capacity. The insert SAED images exhibited concentric rings and indicated that both PB and NO-PB nanoparticles were amorphous. TEM analysis showed that an average diameter of the NO-PB was approximately 40 nm and the PB was around 20 nm. After DOX loading, the diameter of NO-PB slightly increased to approximately 45 nm. The size of the nanoparticles was further validated by the DLS method (Figure 2B). The average diameter of PB and NO-PB was 63 ± 20 nm and 123 ± 46 nm, respectively. And, the diameter of DOX-NO-PB increased to 138 ± 60 nm. The sizes measured by DLS were larger than those observed by TEM, because the DLS method detects the hydrodynamic diameter. The PB, NO-PB and DOX-NO-PB were slightly negatively charged, with the zeta potential value of around −5 mV.

In this study, the successful doping of SNP in the NO-PB was verified by IR spectrum (Figure 2C). The stretching vibration of the cyano group at 2088 cm^{-1} was observed in both the PB and the NO-PB. In addition, the cyano group at 2144 cm^{-1} in the SNP was observed in the NO-PB. It suggests that there are two kinds of CN groups in different chemical environment in the NO-PB, possibly corresponding to the absorption caused by SNP and potassium ferricyanide. These CN peaks were presented at two different wavenumbers, implying that SNP was successfully doped into the NO-PB. The N=O stretching vibration of the free SNP was observed at 1945 cm^{-1} and this peak shifted to 1890 cm^{-1} in the NO-PB. It is known that when nitroso group and the neighbour atom forming a straight structure in SNP, nitroso group corresponds a peak at high wavenumber. If not, then, this peak will shift to lower wavenumber. As a result, the result showed that the NO group in the NO-PB was crooked. The peak of the nitroso group in the NO-PB indicated that the NO was introduced into the crystal structure.

The XRD spectrum was also employed to validate the fabrication of the NO-PB nanoparticles. The XRD patterns shown in Figure 2D (right) displayed eight peaks at 17.5°, 24.8°, 35.4°, 39.8°, 43.7°, 51.0°, 54.3° and 57.5°, corresponding to (200), (220), (400), (420), (422), (440), (442) and (620). Above XRD patterns matched that of $Fe_4(Fe(CN)_6)_3$, indicating that the PB nanoparticles were fabricated. Figure 2D (left) showed that the XRD patterns of NO-PB exhibited six peaks at 17.3°, 24.5°, 34.9°, 39.2°, 50.2° and 56.6°, corresponding to (200), (220), (400), (420), (440) and (620). This XRD patterns matched that of $Fe(Fe(CN)_5)(NO)$. The XRD results suggested that the NO group was introduced into the NO-PB nanoparticles.

The hollow structure of NO-PB was validated by the BET measurement. As shown in the BJH adsorption cumulative pore volume profile (Figure 2E), the average pore diameter of the mesoporous NO-PB was 5.4 nm. The hollow structure may facilitate DOX encapsulation into the NO-PB.

Drug Loading and DOX Release

The drug was encapsulated in the porous structure of the carrier by simply mixing DOX with the NO-PB nanoparticles for 48 h. The encapsulation efficiency was approximately 50%, namely, the mass ratio between DOX and NO-PB was 1:5. The maximum concentration of DOX and NO-PB was 1.5 and 7.5 mg/mL, respectively. The DOX-NO-PB nanoparticles could be simply diluted with

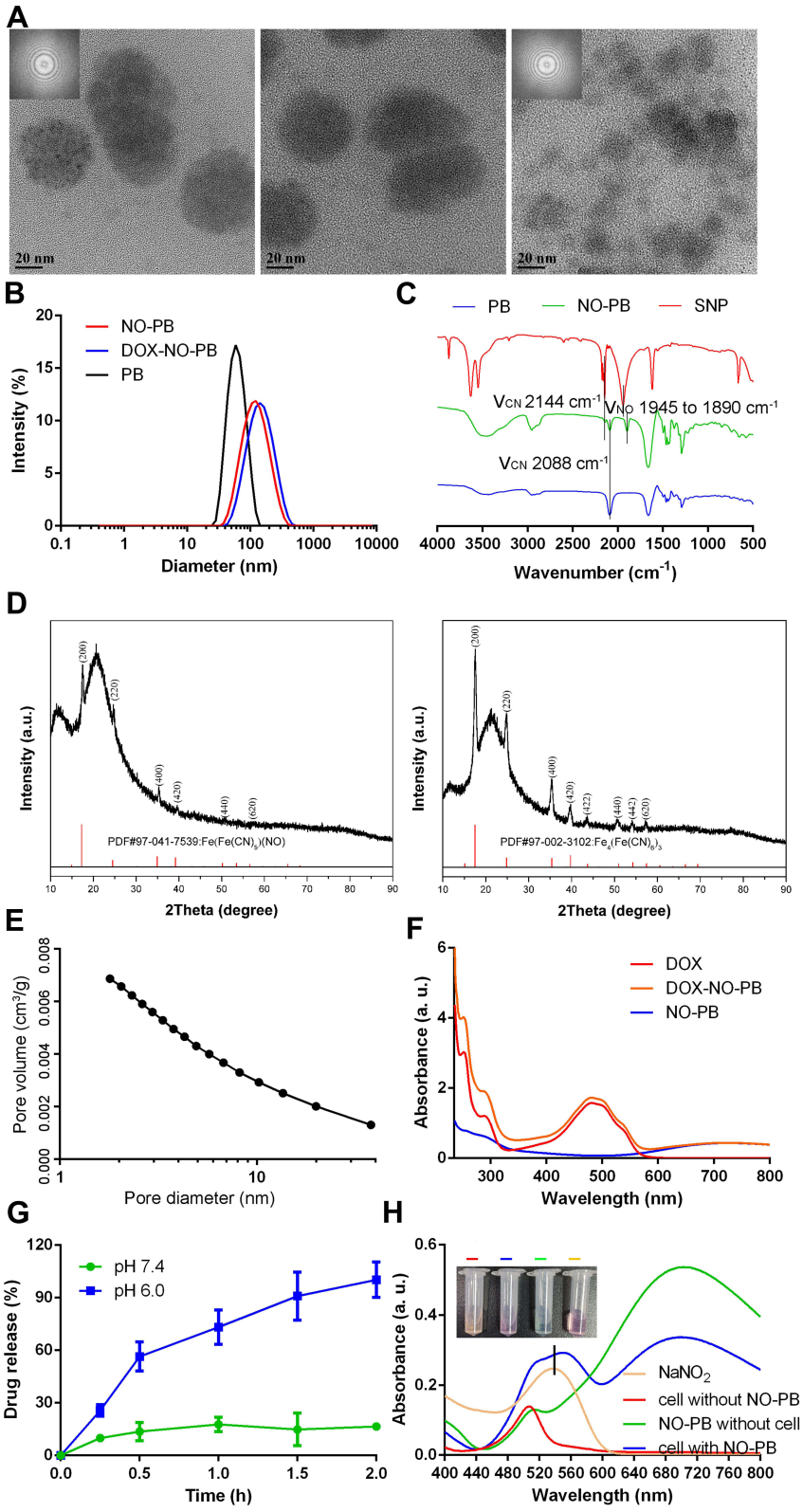

Figure 2 The physical and chemical properties of nanoparticles. (**A**) The TEM and SAED (insert) images of NO-PB (left), DOX-NO-PB (middle) and PB (right) (the scale bar represents 20 nm); (**B**) the particle sizes of NO-PB, DOX-NO-PB and PB measured by the DLS method; (**C**) the IR spectrum of NO-PB, PB and SNP; (**D**) the XRD spectrum of NO-PB (left) and PB (right); (**E**) the BJH adsorption cumulative pore volume profile of NO-PB; (**F**) the UV spectrum of free DOX, NO-PB and DOX-NO-PB; (**G**) the DOX release profiles of DOX-NO-PB in the buffers with pH values of 7.4 and 6.0 (n = 3); (**H**) the NO generation detected by the Griess reagent.

https://doi.org/10.2147/IJN.S327598 DovePress

deionized water or saline to obtain samples with different concentrations. The UV profiles shown in Figure 2F provides an additional evidence for the loading of DOX in NO-PB. Similar to DOX, the DOX-NO-PB had a strong absorbance in the range of 400–560 nm. This absorbance was not observed in the NO-PB. It is worth noting that the NO-PB exhibited a strong absorbance in the range of 550–800 nm, with a peak around 700 nm. The NIR absorbance may confer the capacity of photoacoustic imaging to the nanocarrier, which will be discussed in another section.

The drug release plays a vital role in the antitumor performances. The dissolution test was carried out to measure DOX release. Ideally, the carriers encapsulated DOX are intact in the blood circulation and release DOX specifically in the tumor tissues to improve the antitumor effects and reduce the side-effects. As shown in Figure 2G, the DOX release from DOX-NO-PB was quicker at pH 6.0 compared with neutral pH, with a release rate over 90% after 2 h. In comparison, the release rate was less than 15% at neutral pH. It is widely known that the pH value of the tumor microenvironment is slightly lower than blood and healthy tissues. This nanoparticle may facilitate the release of loaded drug in acidic tumor tissue with limited linkage within neutral environment such as blood circulation and normal tissue.

The NO Production in 4T1 Cells

The principle of gas therapy against tumor is production and release of gas such as NO in tumor tissues or cells. Griess reagent is often used to detect NO molecules. In the presence of NO, the Griess reagent will change from colorless to pink or red, with a maximum absorbance at 535 nm. In order to measure the capacity of NO production by NO-PB, 4T1 cells were incubated with NO-PB and Griess reagent was used to detect the NO release in the culture medium. As shown in Figure 2H, comparable to $NaNO_2$, the conditioned media of 4T1 cells with NO-PB treatment changed to light pink after reaction with the Griess reagent, while the fresh media with NO-PB still displayed the original blue color of NO-PB. The conditioned media of 4T1 cells without NO-PB treatment did not show the color of pink or red, which demonstrated that the cells did not produce NO automatically. In addition, the UV profile of $NaNO_2$ and the conditioned media with NO-PB showed an obvious peak at 535 nm. Both results indicate that the NO-PB can be utilized by 4T1 cells for the generation of NO.

Figure 3A shows the detection of produced NO within 4T1 cells by the fluorescence probe DAF-FM DA. DAF-FM DA is able to diffuse into the cells and metabolize into DAF-FM, which is imprisoned within the cells. The DAF-FM emits green fluorescence after the reaction with NO molecules in the cells. The results showed that there was no apparent NO in the cells without treatment or treated with PB. This suggested that PB irritation alone did not lead to the production of the toxic NO molecules in the cells. In comparison, the cells treated by NO-PB nanoparticles showed a strong NO signal. The results further demonstrated that the NO-PB could release NO molecules in the cells. The results of the fluorescence test were further detected by the flow cytometry. As shown in Figure S1A, the strength of green fluorescence between the control (upper) and PB treated group (middle) was not significantly different. The NO-PB (lower) treated cell showed much stronger green fluorescence compared with PB. Taken together, our results suggested that NO-PB could be metabolized by cells for the production of NO. It was supposed that the NO release in the cells was stimuli-responsive.[44–46] The underlying mechanism needs further investigation.

The Therapeutic Effects Against 4T1 Cells

The live/dead assay was performed to assess the antitumor efficacy of the nanoparticles (Figure 3B). Comparable to the control cells, the dead cells with red fluorescence were rarely detected in PB treated group. This indicated that the good compatibility of Prussian blue with 4T1 cells. In comparison, nearly all the nucleus of cells were stained with red fluorescence, indicating the NO-PB induced cell death. This may be caused by the production of NO by NO-PB as shown by the results from the last section. As the auto-fluorescence of DOX greatly influences the detection, the DOX and DOX-NO-PB groups were not tested. The apoptosis induced by nanoparticles was further detected by the Annexin V-FITC/PI apoptosis assay. As shown in Figure S1B, a small proportion of cells in the control were apoptotic, with 8.32% cells in early stage and 5.48% in late-stage apoptosis. The PB treatment did not increase the percentage of apoptotic cells (middle), with 9.86% in early stage and 6.39% in late-stage apoptosis. The NO-PB treatment (lower) led to obvious increase in cells in both early and late stage of apoptosis, with 17.95% and 76.58%, respectively. In consistence with the results

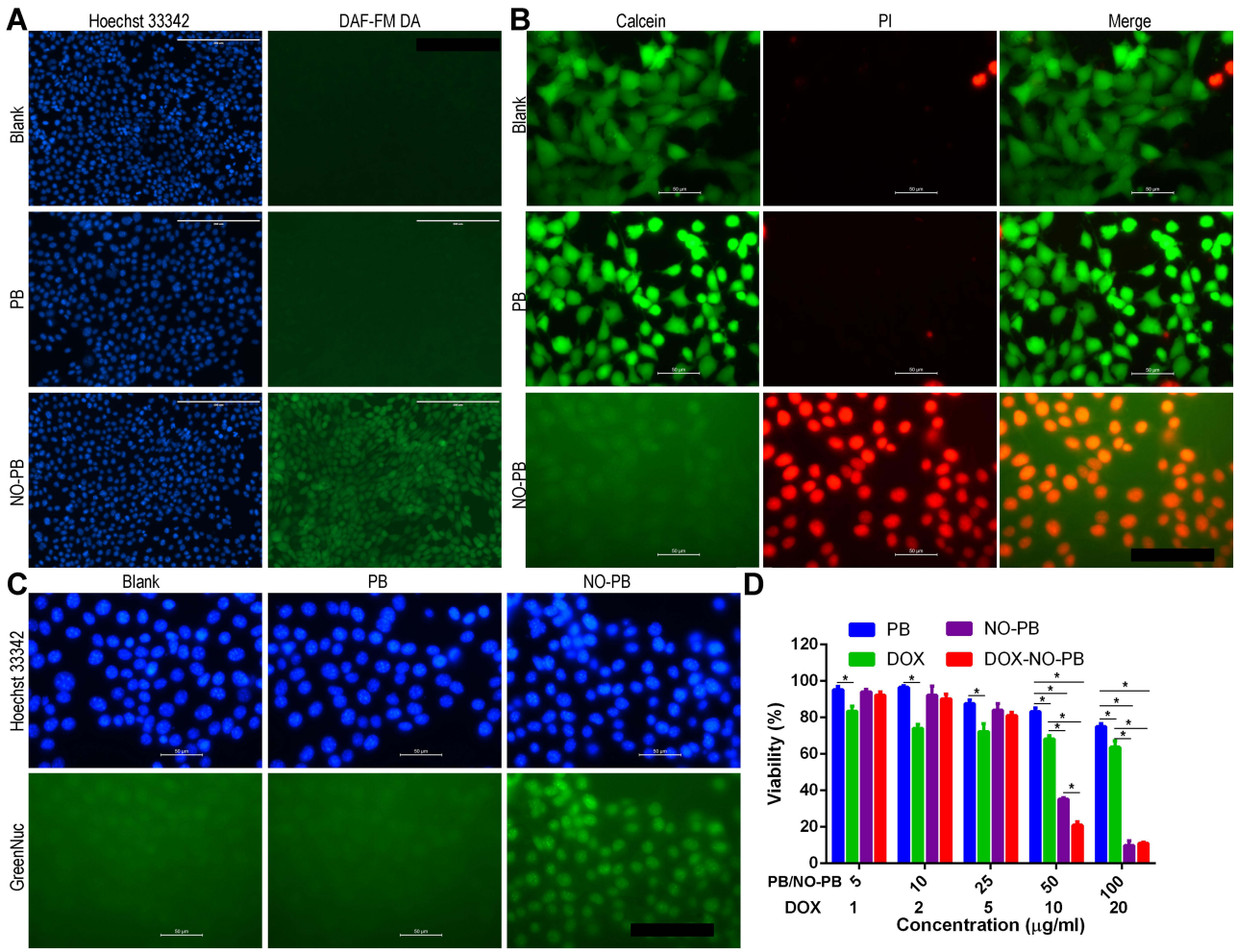

Figure 3 The NO production capacity and anti-tumor effect of nanoparticles in 4T1 cells. (**A**) The NO generation in the 4T1 cells detected by the fluorescence probe DAF-FM DA (the scale bar represents 200 μm); (**B**) the live-dead assay by the Calcein/PI kit (the scale bar represents 100 μm); (**C**) the caspase 3 activation in the 4T1 cells by the GreenNuc kit (the scale bar represents 100 μm); (**D**) the cell viability measured by the MTT test, *Represents statistically significant ($p < 0.05$, $n = 6$).

from live/dead cell staining, NO-PB induced death of tumor cells.

Caspase 3 activation is a hallmark of cell apoptosis. To further evaluate the antitumor efficacy of the NO-PB, the caspase 3 activation in the cells was evaluated by the GreenNuc kit. The detection reagent is a substrate of caspase 3, namely peptide DEVD conjugated with a dye with green fluorescence that can automatically bind to DNA in the nucleus. The negative charge of this substrate limits its entrance into nucleus and binding to DNA. Caspase-3 splice this substrate and produce free DNA dye that can stain DNA with green fluorescence. As shown in Figure 3C, the green fluorescence of nucleus in the control and the PB group was not evident. In contrast, almost all the cells treated by the NO-PB presented green fluorescence within the nucleus. This indicated that NO-PB treatment activated caspase-3 in 4T1 cells, possibly due to the NO production. As the auto-fluorescence of DOX greatly influences the observation, the DOX and DOX-NO-PB groups were not tested.

The MTT test was performed to evaluate the antitumor efficacy quantitatively. As shown in Figure 3D, the PB nanoparticles did not exhibit significant inhibition of tumor cells at the concentration of 10 μg/mL with the cell viability of 96.5%. At even high concentration of 100 μg/mL, only a mild inhibition of cells was observed with 75% cells survived. This suggested a good compatibility of the PB nanoparticles with cells. The drug DOX brought obvious toxicity to the cells, the viability decreased to 73.9% at 2 μg/mL. However, the further increase in concentration did not bring further decrease in the viability, over 60% of the cells still survived at 20 μg/mL. This phenomenon may be induced by the chemotherapy-resistance, in which synergistic therapy is needed. The toxicity of the NO-PB was dose-dependent, the cell viability was 84% at 25 μg/mL and

sharply declined to 35% and 9.8% at 50 and 100 μg/mL. The combination of chemotherapy and NO therapy further improves the antitumor efficacy, with only 20.9% cells survived with the treatment of the DOX-NO-PB containing 50 μg/mL of NO-PB and 10 μg/mL of DOX. These results suggested that the synergistic effects of the combination therapy of NO and DOX on suppression of tumor cells in vitro.

Photoacoustic Imaging (PAI) in vitro and in vivo

As illustrated in Figure 2F and H, the NO-PB nanoparticles had NIR absorbance, which may facilitate their detection by PAI. The imaging capacity of NO-PB nanoparticles in PAI detection was examined in this section. As shown in Figure 4, the negative control, namely deionized water, exhibited negligible photoacoustic signal in vitro. In contrast, the NO-PB displayed strong photoacoustic signal. As anticipated, the result demonstrated that the NO-PB nanoparticles were potential candidate as contrast agent for PAI.

To further validate the potency of the NO-PB nanoparticles in tumor diagnosis by PAI in vivo, the tumor sites were imaged by ultrasound imaging and PAI before and after i.v. administration of NO-PB in tumor bearing mice (Figure 4). The results showed that the intrinsic photoacoustic signal of tumor tissue was very weak without administration of nanoparticles. After i.v. injection of the NO-PB, the photoacoustic signals were observed throughout the entire tumor. This indicated that NO-PB nanoparticles can be accumulated in tumor tissue and may serve as a potential candidate as PAI enhancer for the diagnosis of tumor. PAI has the advantages of high resolution, excellent sensitivity and the ability of real-time imaging. As a potential PAI contrast agent, the NO-PB nanoparticles may be used to monitor the tumor progression and the therapy response in a non-invasive fashion.

The Antitumor Effects in vivo

The therapeutic effects of DOX-NO-PB were tested in the 4T1 breast cancer bearing mouse models. There were four groups including control, free DOX, NO-PB and DOX-NO-PB (one mouse died in the control and free DOX group in the experiment process). The curing effects were assessed in the following aspects: the tumor growth profiles, the tumor weights and the expression of Ki67 and cleaved caspase-3 in the tumor tissues. As shown in Figure 5B, the control group displayed rapid tumor growth, with the final tumor volume reaching about 564 ± 150 mm^3. Moderate inhibition of tumor growth was induced by DOX and the NO-PB alone compared with the control group. The tumors finally grew to 284 ± 76 mm^3 in the DOX group and 263 ± 66 mm^3 in the NO-PB group. This suggested the gas therapy by NO-PB exhibited similar anti-tumor effects with DOX in the present model. The DOX-NO-PB nanoparticles displayed the strongest antitumor effects. The tumor tissues grew slowly

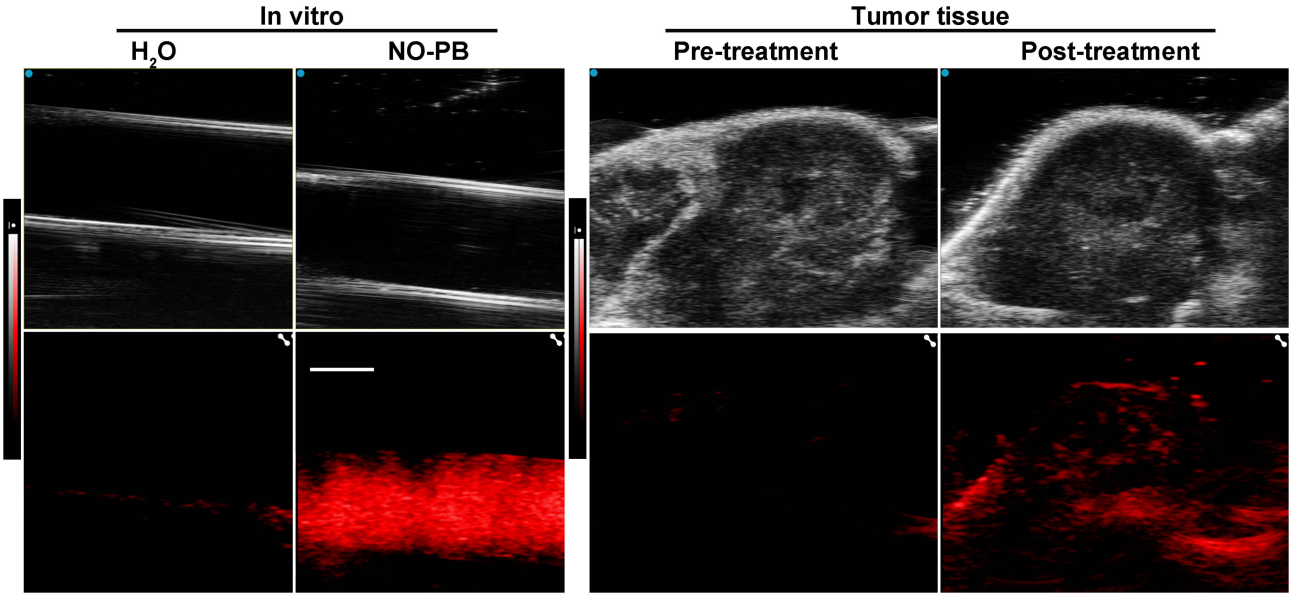

Figure 4 The PAI imaging capacity of NO-PB nanoparticles. The PA images of the deionized water and NO-PB in vitro (the scale bar represents 0.5 mm) as well as in tumor tissues with or without i.v. administration of NO-PB.

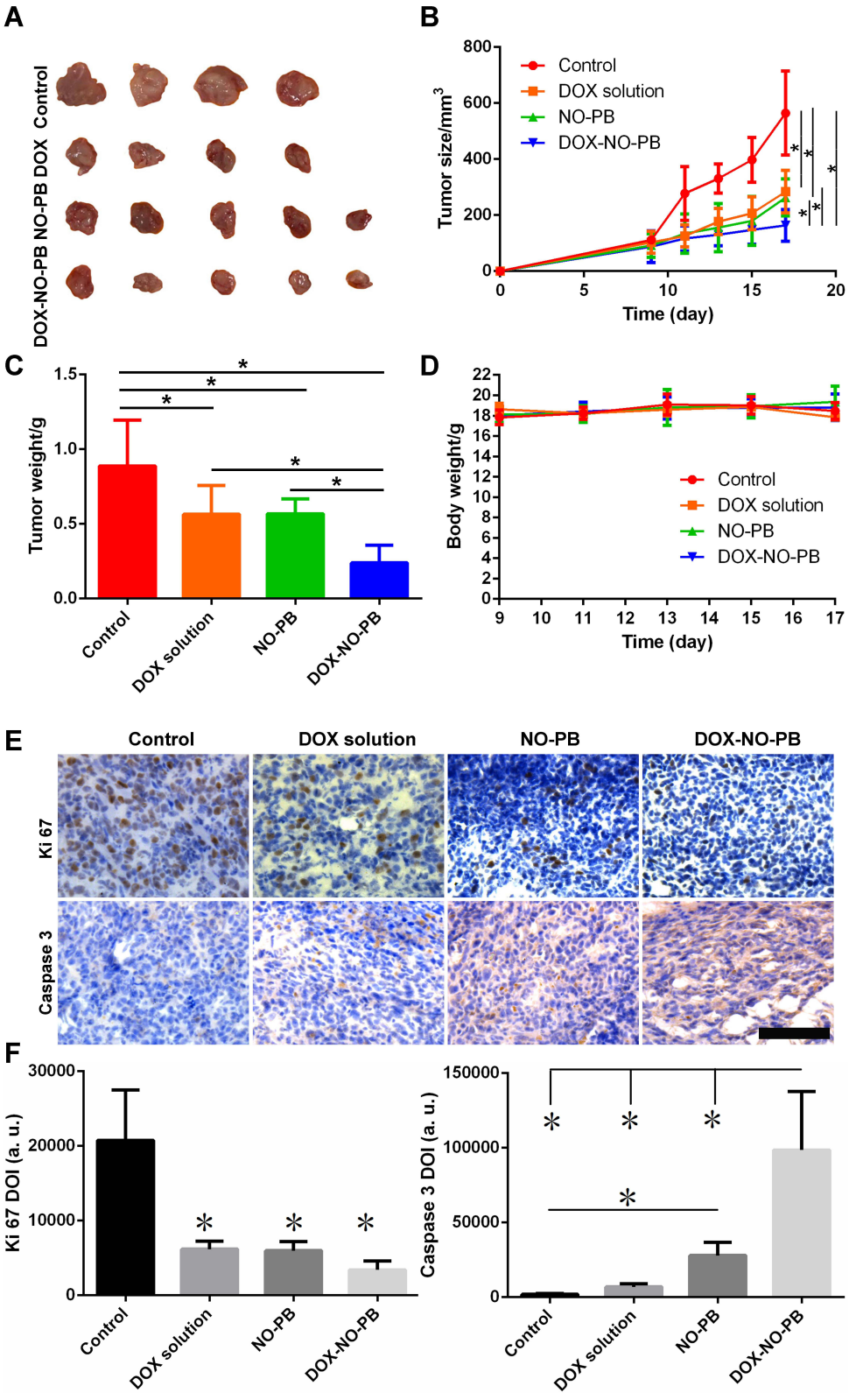

Figure 5 The anti-tumor effects of nanoparticles in 4T1 tumor bearing mice. 4T1 tumor bearing mice were administrated with PBS (as control), free DOX (250 μg/mouse), NO-PB (50 μg/mouse) or DOX-NO-PB (containing 50 μg NO-PB and 250 μg/mouse). (**A**) The picture of the tumor samples (__ represents 1 cm); (**B**) the tumor growth profiles throughout the whole experiment, *Represents statistical difference ($p < 0.05$, $n = 5$); (**C**) the tumor weights at the end of the experiment, *Represents statistical difference ($p < 0.05$, $n = 5$); (**D**) the body weight changes of the mice throughout the experiment ($n = 5$); (**E**) the IHC images of the cleaved caspase 3 and Ki 67 expression in the tumor tissues (the scale bar represents 100 μm); (**F**) the quantitative analysis of the Ki67 and the cleaved caspase 3 expression, *Represents statistical difference ($p < 0.05$, $n = 5$).

https://doi.org/10.2147/IJN.S327598 DovePress

throughout the whole experiment and the final tumor size was 163 ± 57 mm^3. As expected, the combination of DOX chemotherapy and gas therapy displayed synergistic anti-tumor effects. The size of isolated tumor tissue was consistent with the measured tumor size in situ (Figure 5A). The biggest tumors were found in the control group and the tumor sizes in the DOX solution group and the NO-PB group were moderate, the DOX-NO-PB group had the smallest tumor tissues. As one mouse died in the control and the DOX group before the end of the experiment, only four tumor samples were shown in the picture. The tumor samples were weighed to evaluate the antitumor effects quantitatively. The average weights of the control, the DOX solution, the NO-PB, the DOX-NO-PB groups were 0.89 ± 0.31 g, 0.56 ± 0.19 g, 0.57 ± 0.10 g and 0.24 ± 0.12 g (Figure 5C), respectively. The tumor weight in the DOX and the NO-PB groups was significantly lower than the control group and the tumors in the DOX-NO-PB group were lighter than the other three groups.

To further evaluate the therapeutic effects, the IHC experiments were carried out to measure the cleaved caspase 3 and Ki67 expression (Figure 5E). The Ki67 is an important marker of cell proliferation and the cleaved caspase 3 is hallmark of cell apoptosis. The results showed that the Ki67 expression was reduced in DOX, NO-PB and DOX-NO-PB treated mice, of which DOX-NO-PB induced the most significant reduction. In contrast, the cleaved caspase 3 expression was the most obvious in the tumor tissue of DOX-NO-PB treated mice among four groups. The cleaved caspase 3 expression in NO-PB group was higher than the DOX group. The results indicated that the DOX-NO-PB treatment led to most significant apoptosis of tumors, while the NO-PB group and the DOX group exhibited moderate effects. The quantitative analysis of the Ki67 and the cleaved caspase 3 expression is illustrated in Figure 5F. In a word, the DOX and the NO-PB nanoparticles induced cell apoptosis and inhibited cell proliferation in the tumors and, finally, retarded the tumor growth. The combination of chemotherapy and the gas therapy by the DOX-NO-PB nanoparticles showed synergistic therapeutic effects on tumor.

The body weight of mice was monitored to evaluate the systemic toxicity of the treatments. Figure 5D shows that all the groups had a nearly constant body weights throughout the whole experiment. The results implied that the DOX, the NO-PB and the DOX-NO-PB did not cause serious systemic toxicity. To further assess the systemic toxicity, the morphology of main organs of the mice were detected by H & E staining at the end of the experiment (Figure S2). The results showed that all the organs exhibited no obvious morphological changes. This further demonstrated the safety of the DOX-NO-PB nanoparticles combined with chemotherapy and gas therapy.

Conclusions

In this study, SNP-doped hollow mesoporous PB nanoparticles carrying DOX were prepared. The NO moiety was successfully introduced into the PB nanocarriers. The DOX encapsulated in the NO-PB showed pH-dependent drug release, which may improve the tumor-specific toxicity and reduce the systemic toxicity. The NO-PB was able to produce NO molecules in the cells and exhibited anti-tumor effects in 4T1 cells and tumor bearing mice. The NO-PB can be accumulated in tumor tissues and imaged by PAI, suggesting that this nanoparticle may be utilized for non-invasive diagnosis of tumor. The combination of DOX chemotherapy and NO gas showed synergistic effects on tumor suppression with no obvious systemic toxicity.

Abbreviations

MDR, multi-drug resistance; NO, nitric oxide; SNP, sodium nitroprusside; PB, Prussian blue nanoparticles; DOX, doxorubicin; DOX-NO-PB DOX loaded NO-PB; PAI, photoacoustic imaging; CO, carbon monoxide; H_2S, hydrogen sulfide; EMT, epithelial to mesenchymal transition; GSNO, S-nitroglutathione; SNO, S-nitrosothiols; NONOate, N-diazeniumdiolate; L-Arg, L-arginine; SNAP, S-nitroso-N-acetylpenicillamine; NIR, near-infrared; DLS, dynamic light scattering; PVP, polyvinylpyrrolidone; HCl, concentrated hydrochloric acid; SDS, sodium dodecyl sulfate; MTT, 3-(4,5-dimethylthiazol-2-yl)-2,5-diphenyltetrazolium bromide; SAED, Selected area electron diffraction; XRD, X-ray diffraction; IR, infrared spectrum; UV, ultraviolet-visible spectrum; DMEM, Dulbecco's modified Eagle media; IHC, immunohistochemical tests.

Data Sharing Statement

All data used to generate these results is available in the main text.

Ethics Approval and Consent to Participate

The study was approved by Ethics Committee of Guangzhou Medical University.

Acknowledgments

The authors thanks Ping Yuan, Jun-hua Zhou, Sheng-nan Xie, Xiao-xia Ou-yang, Chun-xian Zhou and Xin Huang for their help in this project.

Author Contributions

All authors made substantial contributions to conception and design, acquisition of data, or analysis and interpretation of data; took part in drafting the article or revising it critically for important intellectual content; agreed to submit to the current journal; gave final approval of the version to be published; and agree to be accountable for all aspects of the work.

Funding

This work was supported by the National Natural Science Foundation of China (No. 81803463) and the Natural Science Foundation of Guangdong Province (No. 2018A030310183, 2019A1515110058), Educational Commission of Guangdong Province (2019KQNCX118), Medical Scientific Research Foundation of Guangdong Province (A2020396), the College Student Laboratory Opening Project of Guangzhou Medical University (01-408-2102053) and the High-Level University Construction Fund of Guangdong Province (06-410-2107207, 06-410-2107286).

Disclosure

The authors declare no conflict of interest.

References

1. Wang S-B, Zhang C, Chen Z-X, et al. A versatile carbon monoxide nanogenerator for enhanced tumor therapy and anti-inflammation. *ACS Nano*. 2019;13:5523–5532. doi:10.1021/acsnano.9b00345
2. Yao J, Liu Y, Wang J, et al. On-demand CO release for amplification of chemotherapy by MOF functionalized magnetic carbon nanoparticles with NIR irradiation. *Biomaterials*. 2019;195:51–62. doi:10.1016/j.biomaterials.2018.12.029
3. Yao X, Yang P, Jin Z, et al. Multifunctional nanoplatform for photoacoustic imaging-guided combined therapy enhanced by CO induced ferroptosis. *Biomaterials*. 2019;197:268–283. doi:10.1016/j.biomaterials.2019.01.026
4. Pinto MN, Chakraborty I, Sandoval C, Mascharak PK. Eradication of HT-29 colorectal adenocarcinoma cells by controlled photorelease of CO from a CO-releasing polymer (photoCORP-1) triggered by visible light through an optical fiber-based device. *J Control Release*. 2017;264:192–202. doi:10.1016/j.jconrel.2017.08.039
5. Zhang H, Kong X, Tang Y, Lin W. Hydrogen sulfide triggered charge-reversal micelles for cancer-targeted drug delivery and imaging. *ACS Appl Mater Interfaces*. 2016;8:16227–16239. doi:10.1021/acsami.6b03254
6. Liu Y, Yang F, Yuan C, et al. Magnetic nanoliposomes as in situ microbubble bombers for multimodality image-guided cancer theranostics. *ACS Nano*. 2017;11:1509–1519. doi:10.1021/acsnano.6b06815
7. Shi B, Yan Q, Tang J, et al. Hydrogen sulfide-activatable second near-infrared fluorescent nanoassemblies for targeted photothermal cancer therapy. *Nano Lett*. 2018;18:6411–6416. doi:10.1021/acs.nanolett.8b02767
8. Xie C, Cen D, Ren Z, et al. FeS@BSA nanoclusters to enable H2S-amplified ROS-based therapy with MRI guidance. *Adv Sci*. 2020;7:1903512. doi:10.1002/advs.201903512
9. Liu Y, Li J, Chen H, et al. Magnet-activatable nanoliposomes as intracellular bubble microreactors to enhance drug delivery efficacy and burst cancer cells. *Nanoscale*. 2019;11:18854–18865. doi:10.1039/C9NR07021D
10. Studenovsky M, Sivak L, Sedlacek O, et al. Polymer nitric oxide donors potentiate the treatment of experimental solid tumours by increasing drug accumulation in the tumour tissue. *J Control Release*. 2018;269:214–224. doi:10.1016/j.jconrel.2017.11.017
11. Chen X, Jia F, Li Y, et al. Nitric oxide-induced stromal depletion for improved nanoparticle penetration in pancreatic cancer treatment. *Biomaterials*. 2020;246:119999. doi:10.1016/j.biomaterials.2020.119999
12. Kang Y, Kim J, Park J, et al. Tumor vasodilation by N-Heterocyclic carbene-based nitric oxide delivery triggered by high-intensity focused ultrasound and enhanced drug homing to tumor sites for anti-cancer therapy. *Biomaterials*. 2019;217:119297. doi:10.1016/j.biomaterials.2019.119297
13. Dong X, Liu H-J, Feng H-Y, et al. Enhanced drug delivery by nanoscale integration of a nitric oxide donor to induce tumor collagen depletion. *Nano Lett*. 2019;19:997–1008. doi:10.1021/acs.nanolett.8b04236
14. Guo R, Tian Y, Wang Y, Yang W. Near-infrared laser-triggered nitric oxide nanogenerators for the reversal of multidrug resistance in cancer. *Adv Funct Mater*. 2017;27:1606398. doi:10.1002/adfm.201606398
15. Kim J, Yung BC, Kim WJ, Chen X. Combination of nitric oxide and drug delivery systems: tools for overcoming drug resistance in chemotherapy. *J Control Release*. 2017;263:223–230. doi:10.1016/j.jconrel.2016.12.026
16. Stewart GD, Nanda J, Katz E, et al. DNA strand breaks and hypoxia response inhibition mediate the radiosensitisation effect of nitric oxide donors on prostate cancer under varying oxygen conditions. *Biochem Pharmacol*. 2011;81:203–210. doi:10.1016/j.bcp.2010.09.022
17. Royle JS, Ross JA, Ansell IAN, Bollina P, Tulloch DN, Habib FK. Nitric oxide donating nonsteroidal anti-inflammatory drugs induce apoptosis in human prostate cancer cell systems and human prostatic stroma via caspase-3. *J Urol*. 2004;172:338–344. doi:10.1097/01.ju.0000132367.02834.41
18. Baritaki S, Huerta-Yepez S, Sahakyan A, et al. Mechanisms of nitric oxide-mediated inhibition of EMT in cancer: inhibition of the metastasis-inducer snail and induction of the metastasis-suppressor RKIP. *Cell Cycle*. 2010;9:4931–4940. doi:10.4161/cc.9.24.14229
19. Li B, Ji P, Peng S-Y, et al. Nitric oxide release device for remote-controlled cancer therapy by wireless charging. *Adv Mater*. 2020;32:2000376. doi:10.1002/adma.202000376
20. Lin Y-J, Chen -C-C, Nguyen D, et al. Biomimetic engineering of a scavenger-free nitric oxide-generating/delivering system to enhance radiation therapy. *Small*. 2020;16:2000655. doi:10.1002/smll.202000655
21. Yu Y-T, Shi S-W, Wang Y, et al. A ruthenium nitrosyl-functionalized magnetic nanoplatform with near-infrared light-controlled nitric oxide delivery and photothermal effect for enhanced antitumor and antibacterial therapy. *ACS Appl Mater Interfaces*. 2020;12:312–321. doi:10.1021/acsami.9b18865
22. Baek S, Singh RK, Khanal D, et al. Smart multifunctional drug delivery towards anticancer therapy harmonized in mesoporous nanoparticles. *Nanoscale*. 2015;7:14191–14216. doi:10.1039/C5NR02730F

23. Deng Y, Jia F, Chen X, Jin Q, Ji J. ATP suppression by pH-activated mitochondria-targeted delivery of nitric oxide nanoplatform for drug resistance reversal and metastasis inhibition. *Small*. 2020;16:2001747. doi:10.1002/smll.202001747
24. Fan J, He N, He Q, et al. A novel self-assembled sandwich nanomedicine for NIR-responsive release of NO. *Nanoscale*. 2015;7:20055–20062. doi:10.1039/C5NR06630A
25. Huang X, Xu F, Hou H, Hou J, Wang Y, Zhou S. Stimuli-responsive nitric oxide generator for light-triggered synergistic cancer photothermal/gas therapy. *Nano Res*. 2019;12:1361–1370. doi:10.1007/s12274-019-2307-x
26. Jiang L, Ding Y, Xue X, et al. Entrapping multifunctional dendritic nanoparticles into a hydrogel for local therapeutic delivery and synergetic immunochemotherapy. *Nano Res*. 2018;11:6062–6073. doi:10.1007/s12274-018-2123-8
27. Jin Z, Wen Y, Hu Y, et al. MRI-guided and ultrasound-triggered release of NO by advanced nanomedicine. *Nanoscale*. 2017;9:3637–3645. doi:10.1039/C7NR00231A
28. Li X, Zhang Y, Sun J, et al. Protein nanocage-based photo-controlled nitric oxide releasing platform. *ACS Appl Mater Interfaces*. 2017;9:19519–19524. doi:10.1021/acsami.7b03962
29. Rolim WR, Pieretti JC, Renó DLS, et al. Antimicrobial activity and cytotoxicity to tumor cells of nitric oxide donor and silver nanoparticles containing PVA/PEG films for topical applications. *ACS Appl Mater Interfaces*. 2019;11:6589–6604. doi:10.1021/acsami.8b19021
30. Sudhesh P, Tamilarasan K, Arumugam P, Berchmans S. Nitric oxide releasing photoresponsive nanohybrids as excellent therapeutic agent for cervical cancer cell lines. *ACS Appl Mater Interfaces*. 2013;5:8263–8266. doi:10.1021/am402086m
31. Sun Z, Yi Z, Cui X, et al. Tumor-targeted and nitric oxide-generated nanogels of keratin and hyaluronan for enhanced cancer therapy. *Nanoscale*. 2018;10:12109–12122. doi:10.1039/C8NR03265C
32. Xu Y, Ren H, Liu J, et al. A switchable NO-releasing nanomedicine for enhanced cancer therapy and inhibition of metastasis. *Nanoscale*. 2019;11:5474–5488. doi:10.1039/C9NR00732F
33. Zhang X, Tian G, Yin W, et al. Controllable generation of nitric oxide by near-infrared-sensitized upconversion nanoparticles for tumor therapy. *Adv Funct Mater*. 2015;25:3049–3056. doi:10.1002/adfm.201404402
34. Zhang K, Xu H, Jia X, et al. Ultrasound-triggered nitric oxide release platform based on energy transformation for targeted inhibition of pancreatic tumor. *ACS Nano*. 2016;10:10816–10828. doi:10.1021/acsnano.6b04921
35. Zhang H, Tian X-T, Shang Y, Li Y-H, Yin X-B. Theranostic Mn-porphyrin metal–organic frameworks for magnetic resonance imaging-guided nitric oxide and photothermal synergistic therapy. *ACS Appl Mater Interfaces*. 2018;10:28390–28398. doi:10.1021/acsami.8b09680
36. Zhang J, Song H, Ji S, et al. NO prodrug-conjugated, self-assembled, pH-responsive and galactose receptor targeted nanoparticles for co-delivery of nitric oxide and doxorubicin. *Nanoscale*. 2018;10:4179–4188. doi:10.1039/C7NR08176F
37. Jia X, Cai X, Chen Y, et al. Perfluoropentane-encapsulated hollow mesoporous Prussian blue nanocubes for activated ultrasound imaging and photothermal therapy of cancer. *ACS Appl Mater Interfaces*. 2015;7:4579–4588. doi:10.1021/am507443p
38. Zhang K, Tu M, Gao W, et al. Hollow Prussian blue nanozymes drive neuroprotection against ischemic stroke via attenuating oxidative stress, counteracting inflammation, and suppressing cell apoptosis. *Nano Lett*. 2019;19(5):2812–2823. doi:10.1021/acs.nanolett.8b04729
39. Chen W, Zeng K, Liu H, et al. Cell membrane camouflaged hollow Prussian blue nanoparticles for synergistic photothermal-/chemotherapy of cancer. *Adv Funct Mater*. 2017;27(11):1605795. doi:10.1002/adfm.201605795
40. Cheng L, Gong H, Zhu W, et al. PEGylated Prussian blue nanocubes as a theranostic agent for simultaneous cancer imaging and photothermal therapy. *Biomaterials*. 2014;35:9844–9852. doi:10.1016/j.biomaterials.2014.09.004
41. Jing L, Liang X, Deng Z, et al. Prussian blue coated gold nanoparticles for simultaneous photoacoustic/CT bimodal imaging and photothermal ablation of cancer. *Biomaterials*. 2014;35(22):5814–5821. doi:10.1016/j.biomaterials.2014.04.005
42. Sahu A, Lee JH, Lee HG, Jeong YY, Tae G. Prussian blue/serum albumin/indocyanine green as a multifunctional nanotheranostic agent for bimodal imaging guided laser mediated combinatorial phototherapy. *J Control Release*. 2016;236:90–99. doi:10.1016/j.jconrel.2016.06.031
43. Tian W, Su Y, Tian Y, et al. Periodic mesoporous organosilica coated Prussian blue for MR/PA dual-modal imaging-guided photothermal-chemotherapy of triple negative breast cancer. *Adv Sci*. 2017;4:1600356. doi:10.1002/advs.201600356
44. Wu Y, Li F, Zhang X, et al. Tumor microenvironment-responsive PEGylated heparin-pyropheophorbide-a nanoconjugates for photodynamic therapy. *Carbohydr Polym*. 2021;255:117490. doi:10.1016/j.carbpol.2020.117490
45. Cai H, Xiang Y, Zeng Y, et al. Cathepsin B-responsive and gadolinium-labeled branched glycopolymer-PTX conjugate-derived nanotheranostics for cancer treatment. *Acta Pharm Sin B*. 2021;11:544–559. doi:10.1016/j.apsb.2020.07.023
46. Pan D, Zheng X, Zhang Q, et al. Dendronized-polymer disturbing cells‘ stress protection by targeting metabolism leads to tumor vulnerability. *Adv Mater*. 2020;32(14):1907490. doi:10.1002/adma.201907490